Research Article | Vol. 12, No. 12 / 1 Dec 2021 / *Biomedical Optics Express* 7807

Biomedical Optics EXPRESS

L1-L2 norm regularization via forward-backward splitting for fluorescence molecular tomography

HENG ZHANG,[1,2] XIAOWEI HE,[1,2] JINGJING YU,[3] XUELEI HE,[1,2] HONGBO GUO,[1,2,4] AND YUQING HOU[1,2,5]

[1]*The Xi'an Key Laboratory of Radiomics and Intelligent Perception, Xi'an, China*
[2]*School of Information Sciences and Technology, Northwest University, Xi'an, 710127, China*
[3]*School of Physics and Information Technology, Shaanxi Normal University, Xi'an, 710062, China*
[4]*Guohb@nwu.edu.cn*
[5]*houyuqin@nwu.edu.cn*

Abstract: Fluorescent molecular tomography (FMT) is a highly sensitive and noninvasive imaging approach for providing three-dimensional distribution of fluorescent marker probes. However, owing to its light scattering effect and the ill-posedness of inverse problems, it is challenging to develop an efficient reconstruction algorithm that can achieve the exact location and morphology of the fluorescence source. In this study, therefore, in order to satisfy the need for early tumor detection and improve the sparsity of solution, we proposed a novel L_1-L_2 norm regularization via the forward-backward splitting method for enhancing the FMT reconstruction accuracy and the robustness. By fully considering the highly coherent nature of the system matrix of FMT, it operates by splitting the objective to be minimized into simpler functions, which are dealt with individually to obtain a sparser solution. An analytic solution of L_1-L_2 norm proximal operators and a forward-backward splitting algorithm were employed to efficiently solve the nonconvex L_1-L_2 norm minimization problem. Numerical simulations and an *in-vivo* glioma mouse model experiment were conducted to evaluate the performance of our algorithm. The comparative results of these experiments demonstrated that the proposed algorithm obtained superior reconstruction performance in terms of spatial location, dual-source resolution, and *in-vivo* practicability. It was believed that this study would promote the preclinical and clinical applications of FMT in early tumor detection.

1. Introduction

With the development of medical imaging technology, fluorescence molecular imaging (FMI) has widely applied in the study of drug delivery, protein function, preclinical, clinical, etc. [1–5]. However, FMI can only obtain the photon intensity of the object surface because of the absorption and scattering of light transmission. Therefore, fluorescence molecular tomography (FMT), which can accurately visualize and quantify the three-dimensional (3D) distribution of fluorescent sources in deep turbidities by capturing the surface fluorescence distribution of fluorescence sources using an ultra-sensitive charge-coupled device (CCD) camera, is favored by researchers [6–8].

However, owing to the strong scattering property of biological tissues and the limited boundary measurements with noise, FMT reconstruction is always an ill-posed problem [9,10]. Moreover, the mutual coherence of system matrix derived by finite element method (FEM) is always as high as above 90%, which also increase the complexity of FMT reconstruction [11]. Thus, the reconstruction is still a challenging problem [12–14]. Over the past few years, many reconstruction methods have been developed to reduce the ill-posedness [15–17]. Tikhonov regularization have widely used to overcome ill-posedness by adding L_2 norm [18]. The primary benefit of using L_2 norm is the simplicity of the optimization problem. However, it causes over-smoothing, leading to a blurring of the sources and making it difficult to obtain sharp boundaries [19].

#435932 https://doi.org/10.1364/BOE.435932
Journal © 2021 Received 6 Jul 2021; revised 8 Nov 2021; accepted 8 Nov 2021; published 29 Nov 2021

Biomedical Optics EXPRESS

FMT is usually utilized for early tumor imaging, and in this stage the tumor is always small and sparse in size compared to the entire body of the subject [20,21]. Mathematically speaking, the L_0 norm is the sparsest constrain. The reconstruction algorithm based on the L_0 norm regularization algorithm involves a problem of combinatory optimization, which makes it inefficient or unfeasible for practical applications. Thus, to improve the quality of the reconstruction, convex L_1 norm regularization has been adopted in FMT reconstruction. Several algorithms based on the L_1 norm have been proposed for optical molecular imaging and allow for more accurate results and less computation time, such as the iterated shrinkage algorithm with the L_1 norm [22], fast iterative soft-thresholding algorithm [23] , L_1 norm regularization algorithm based on the split Bregman algorithm [24,25], gradient-based techniques, and the incomplete variable truncated conjugate gradient algorithm. Moreover, the algorithm based on the L_1 norm can obtain satisfactory results and overcome the over-smoothing cause by the L_2 norm.

Recently, some novel regularization algorithm base on non-convex L_p norm ($0<p<1$) have been proposed. For example, He et al. proposed the half thresholding pursuit algorithm, with significant improvements in achieving the accuracy and sparse for the reconstruction of FMT [26]. In addition, Guo et al. proposed a non-convex sparse regularization approach (nCSRA) framework, which have a better multiple-source resolution capability in terms of position resolution, intensity resolution and size resolution [27]. Compared with the L_1 norm, the L_p norm ($0<p<1$) is a better approximation of the L_0 norm. Thus, an algorithm based on L_p norm can always obtain a sparser solution compared with L_1 norm algorithms, thus ensuring stability at the same time.

Recently, it was demonstrated in a series of papers that the difference of the L_1 norm and L_2 norm (L_1-L_2 norm), outperforms L_1 norm and L_p norm in terms of promoting sparsity when system matrix is highly coherent [28]. Inspired by this, L_1-L_2 norm regulation via difference of convex algorithm (L_1-L_2 via DCA) algorithm, has been used in FMT reconstruction having a great improvement in the sparsity of the solution [29]. However, the L_1-L_2 via DCA algorithm decomposes the objective function as the difference of two convex functions, convert to L_1 norm minimization problem, which may not have analytical solutions. Thus, the robustness of L_1-L_2 via DCA algorithm is therefore poor, especially for multiple sources resolution. Furthermore, because the L_1-L_2 via DCA algorithm for L_1-L_2 amounts to solving an L_1 norm minimization problem iteratively as a subproblem, it is much slower than L_1 norm minimization [30].In recently years, forward-backward splitting (FBS) method has been proposed to solve the nonlinear and nonconvex least-squares problem with tight frame sparsity regularization in quantitative photoacoustic tomography [31] and Low-dose CT [32]. These research prove the convergence and efficiency of FBS, and provide a proximal operator of the L_1-L_2 metric.

To satisfy the need for early tumor detection in FMT, a novel L_1-L_2 norm regularization algorithm via forward-backward splitting (L_1-L_2 via FBS) algorithm was proposed to recover the distribution of small fluorescent sources in orthotopic glioma mouse models. First, L_1-L_2 via FBS algorithm employ proximity operators and gradient descent to obtain the search point. It is worth mentioning that we derive an analytical solution for the proximal operator of the L_1-L_2 norm. Second, they operate by splitting the objective to be minimized into simpler functions that are dealt with individually to get a sparser solution. Thus, the main advantages of L_1-L_2 via FBS algorithm is full considering the highly coherent of the system matrix of FMT and the handling of non-differentiable objectives and non-convex constraints due to the L_1-L_2 norm while maintaining the simplicity of gradient descent methods and the sparsity of results. To validate the performance of the proposed algorithm, groups of comparison experiments were designed using numerical simulations and *in-vivo* imaging experiments for the L_1-L_2 via DCA algorithm [29], the incomplete variables truncated conjugate gradient algorithm (IVTCG) based on L_1 norm [33], and $L_{1/2}$ norm regulation based on Iterative shrinkage-thresholding algorithm (ISTA-$L_{1/2}$)

Biomedical Optics EXPRESS

[27]. It has experimentally shown that the proposed L_1-L_2 via FBS algorithm performance better in spatial location, dual-source resolution, robustness, and *in-vivo* practicability.

2. Materials and methods

2.1. Photon propagation model

In biological bodies, photon propagation within the near-infrared spectral band has a highly scattering feature. For steady-state FMT with point excitation sources, the following coupled diffusion equations (DE) have been commonly used to model the forward problem of FMT, which is defined as [34–36]:

$$\begin{cases} \nabla \cdot (D_x(\mathbf{r})\nabla\Phi_x(\mathbf{r}) - \mu_{ax}\Phi_x(\mathbf{r})) = -\Theta_s\delta(\mathbf{r}-\mathbf{r}_l) \\ \nabla \cdot (D_m(\mathbf{r})\nabla\Phi_m(\mathbf{r}) - \mu_{am}\Phi_m(\mathbf{r})) = -\Phi_x(\mathbf{r})\eta\mu_{af}(\mathbf{r}) \end{cases} \quad \mathbf{r}\in\Omega \tag{1}$$

where subscripts x and m denote the excitation and emission light respectively. Φ_x stands for the photon flux density, $D_{x,m}$ denote the diffusion coefficient in biological tissues, $D_{x,m} = 1/3[\mu_{ax,am} + (1-g)\mu_{sx,sm}]$, where $\mu_{ax,am}$ and $\mu_{sx,sm}$ represent the absorption coefficient and scattering coefficient respectively, and g is the anisotropy parameter; $\eta\mu_{af}(\mathbf{r})$ represents the unknown fluorescence yield distribution to be reconstructed, $\Theta_s\delta(\mathbf{r}-\mathbf{r}_l)$ denotes the excitation light which is considered as the point source. $\mathbf{r}_l$ represents the position of a point source with an amplitude of Θ_s. $\delta(\mathbf{r})$ is the Dirac function.

To solve these equations, the Robin-type boundary conditions are added on the boundary $\partial\Omega$ of the domain Ω [37]:

$$2D_{x,m}\partial\Phi_{x,m}/\partial\mathbf{n} + q\Phi_{x,m} = 0 \tag{2}$$

where $\mathbf{n}$ represents the outward normal vector to the surface. q is a constant depending on the optical reflective index mismatch at the boundary.

Based on FEM method, we can obtain the following linear model:

$$\mathbf{Ax} = \mathbf{\Phi} \tag{3}$$

where $\mathbf{A}$ is an $M \times N$ weighting matrix, and $\mathbf{x}$ is an $N \times 1$ vector denotes the unknown internal distribution of the probes, $\mathbf{\Phi}$ is an $M \times 1$ vector represents the measurements of surface photon distribution.

2.2. Reconstruction Based on the forward-backward splitting (FBS) algorithm

In order to alleviate the ill-posedness of the inverse problem, the L_1-L_2 norm regularization was adopted in FMT inverse problem, writing as:

$$\min_{x\in R} \frac{1}{2}||\mathbf{Ax}-\mathbf{\Phi}||_2^2 + \lambda(||\mathbf{x}||_1 - ||\mathbf{x}||_2) \tag{4}$$

where λ is the regulation parameter. Eq. (4) be expressed as

$$\min_{x\in R} \frac{1}{2}f(\mathbf{x}) + \mathrm{g}(\mathbf{x}) \tag{5}$$

where:

$$\begin{aligned} f(\mathbf{x}) &= \tfrac{1}{2}||\mathbf{Ax}-\mathbf{\Phi}||_2^2 \\ \mathrm{g}(\mathbf{x}) &= \lambda(||\mathbf{x}||_1 - ||\mathbf{x}||_2) \end{aligned} \tag{6}$$

Obviously, $f(\mathbf{x})$ is differentiable convex function; however $g(\mathbf{x})$ is no-convex function and nondifferentiable, Eq. (5) cannot be minimized using simple gradient descent methods. For this, a forward-backward splitting (FBS) method was adopted to address each term in Eq. (5).

Biomedical Optics EXPRESS

In the first stage, for improving the computational speed, the search point $\mathbf{s}_k$, was determined by forward splitting, which can be obtained as follows:

$$\mathbf{s}_k = \mathbf{x}_{k-1} - t_{k-1} f'(\mathbf{x}_{k-1}) \tag{7}$$

where $f'(\mathbf{x}) = \mathbf{A}(\mathbf{A}\mathbf{x} - \mathbf{\Phi})$ denotes the gradient of $f(\mathbf{x})$ at the point $\mathbf{x}$; and t_k is the step size. and utilize the Lipschitz condition to get the value of t_k [38].

In the second stage, to ensure global convergence, an approximate solution $\mathbf{x}$, and without straying too far from a starting point $\mathbf{s}_k$. It can be through the proximal operator of g($\mathbf{x}$) obtained:

$$\begin{aligned} \mathbf{x}_k \in prox_{tg}(\mathbf{s}_k) &= \arg\min \tfrac{1}{2t_k}||\mathbf{x} - \mathbf{s}_k||^2 + \mathrm{g}(\mathbf{x}) \\ &= \arg\min \tfrac{1}{2\sigma}||\mathbf{x} - \mathbf{s}_k||^2 + ||\mathbf{x}||_1 - ||\mathbf{x}||_2 \end{aligned} \tag{8}$$

where $\sigma = t_k\lambda$; Define $\mathbf{x}^*$ as the optimal solution. In FMT, because of the non-negative constraint of the unknow source, the non-negative constraint is placed on the vectors, $\mathbf{s}_k^i \geq 0, \quad \mathbf{x}_i^* \geq 0$. Let $G(\mathbf{x}) = \frac{1}{2\sigma}||\mathbf{x} - \mathbf{s}_k||_2^2 + ||\mathbf{x}||_1 - ||\mathbf{x}||_2$, and $G'(\mathbf{x})$ be the derivative of $G(\mathbf{x})$, then for all $\mathbf{x} \neq 0$:

$$G'(\mathbf{x}) = \frac{1}{\sigma}(\mathbf{x} - \mathbf{s}_k) + \mathbf{q} - \frac{\mathbf{x}}{||\mathbf{x}||_2} \tag{9}$$

when $G'(\mathbf{x}) = 0$, we can get:

$$(1 - \frac{\sigma}{||\mathbf{x}||_2})\mathbf{x} = \mathbf{s}_k - \sigma\mathbf{q} \quad for \quad \mathbf{x} \neq 0 \tag{10}$$

where $\mathbf{q} \in \partial||\mathbf{x}||_1$ is a subgradient of the L_1 norm:

$$\mathbf{q} = \partial||\mathbf{x}||_1 = sign(\mathbf{x}) = \begin{cases} 1 & if \quad \mathbf{x}_i > 0 \\ -1 & if \quad \mathbf{x}_i < 0 \\ [1, -1] & for \quad \mathbf{x}_i = 0 \end{cases} \tag{11}$$

For any satisfying Eq. (9), we can obtain $\mathbf{s}_k = \sigma\mathbf{q} + (1 - \frac{\sigma}{||\mathbf{x}||_2})\mathbf{x}$. And through a simple calculation, we have:

$$\begin{aligned} G(\mathbf{x}) &= \frac{1}{2\sigma}||\mathbf{x}||_2^2 - \frac{1}{\sigma}<\mathbf{x}, \mathbf{s}_k> + \frac{1}{2\sigma}||\mathbf{s}_k||_2^2 + ||\mathbf{x}||_1 - ||\mathbf{x}||_2 \\ &= \frac{1}{2\sigma}||\mathbf{x}||_2^2 - \frac{1}{\sigma}<\mathbf{x}, \sigma\mathbf{q} + (1 - \frac{\sigma}{||\mathbf{x}||_2})\mathbf{x}> + \frac{1}{2\sigma}||\mathbf{s}_k||_2^2 + ||\mathbf{x}||_1 - ||\mathbf{x}||_2 \\ &= \frac{1}{2\sigma}||\mathbf{x}||_2^2 - (\frac{1}{\sigma} - \frac{1}{||\mathbf{x}||_2})||\mathbf{x}||_2^2 + \frac{1}{2\sigma}||\mathbf{s}_k||_2^2 - ||\mathbf{x}||_2 \\ &= -\frac{1}{2\sigma}||\mathbf{x}||_2^2 + \frac{1}{2\sigma}||\mathbf{s}_k||_2^2 < G(\mathbf{0}) \end{aligned} \tag{12}$$

Therefore, the $\mathbf{x}^*$ can be determined among all $\mathbf{x}$ satisfying Eq. (10) with the largest norm. Without loss of generality ${\mathbf{s}_k}^i$ is a non-increasing vector, ${\mathbf{s}_k}^1 \geq {\mathbf{s}_k}^2 \geq \cdots \geq {\mathbf{s}_k}^i \geq 0$, then we discuss the optimal solution $\mathbf{x}^*$:

1) When ${\mathbf{s}_k}^1 > \sigma$, then ${\mathbf{s}_k}^1 - \sigma\mathbf{q}_1 > 0$. For $i = 1$, the right-hand side (RHS) of Eq. (10) is positive, so the left-hand side (LHS) is positive as well; owing to the non-negative constraint on the unknown vector, we obtain $(1 - \frac{\sigma}{||\mathbf{x}||_2}) > 0$. For this i, which ${\mathbf{s}_k}^i \leq \sigma$, we have $\mathbf{x}_i^* = 0$; Otherwise for this i, the LHS of Eq. (10) is positive, while the RHS is nonpositive. For this i which ${\mathbf{s}_k}^i > \sigma$,

we have $\mathbf{q}_i = 1$. Thus, for RHS of Eq. (10):$\mathbf{s}_k - \sigma\mathbf{q} = soft(\mathbf{s}_k, \sigma)$; $soft(\mathbf{s}_k, \sigma)$ is the proximal operator of L_1 norm regularized, appoint $\mathbf{z} = soft(\mathbf{s}_k, \sigma)$, and defined as Eq. (13).

$$\begin{aligned}&\mathbf{z} = soft(\mathbf{s}_k, \sigma) = sign(\mathbf{s}_k)(|\mathbf{s}_k| - \sigma)\\&sign(\mathbf{s}_k) = 1 \quad if \quad \mathbf{s}_k>0, sign(\mathbf{s}_k) = -1 \quad if \quad \mathbf{s}_k<0\end{aligned} \tag{13}$$

Do a simple operation on Eq. (10):

$$\begin{aligned}&(1 - \frac{\sigma}{||\mathbf{x}||_2})\mathbf{x} = \mathbf{z}\\&||\mathbf{x} - \frac{\sigma\mathbf{x}}{||\mathbf{x}||_2}||_2 = ||\mathbf{z}||_2\\&||(\mathbf{x}||\mathbf{x}||_2 - \sigma\mathbf{x})||_2 = ||\mathbf{z}||_2||\mathbf{x}||_2\\&||\mathbf{x}||_2 = ||\mathbf{z}||_2 + \sigma\\&\mathbf{x}^* = \frac{\mathbf{z}}{1 - \frac{\sigma}{||\mathbf{x}||_2}} = \frac{||\mathbf{x}||_2}{||\mathbf{x}||_2 - \sigma}\mathbf{z} = \frac{||\mathbf{z}||_2 + \sigma}{||\mathbf{z}||_2}\mathbf{z} = (1 + \frac{\sigma}{||\mathbf{z}||_2})\mathbf{z}\end{aligned} \tag{14}$$

2) When ${\mathbf{s}_k}^1 \leq \sigma$, for this i which ${\mathbf{s}_k}^i<||\mathbf{s}_k||_\infty$, we have $\mathbf{x}^* = 0$, Otherwise for this i, RHS of Eq. (10) is negative, thus $(1-\frac{\sigma}{||\mathbf{x}||_2})<0$, and ${\mathbf{s}_k}^1-\sigma\mathbf{q}_1 = (1-\frac{\sigma}{||\mathbf{x}^*||_2})\mathbf{x}_1^* \leq (1-\frac{\sigma}{||\mathbf{x}^*||_2})\mathbf{x}_i^* = {\mathbf{s}_k}^i-\sigma\mathbf{q}_i$, which is a contradiction to ${\mathbf{s}_k}^1>{\mathbf{s}_k}^i$. For $\mathbf{x}^* \neq 0$, from Eq. (10), we can get: $\sigma-||\mathbf{x}||_2 = ||\mathbf{s}_k-\sigma\mathbf{q}||_2$. And finding $||\mathbf{x}^*||_\infty$ is equivalent to looking for the minimum value of $||\mathbf{s}_k - \sigma\mathbf{q}||_2$ and $\mathbf{x}^* \neq 0$. So, choose $\mathbf{x}^*$ is a 1-sparse vector, then can get $||\mathbf{x}^*||_2 = \mathbf{x}^* = \sigma - ||\mathbf{s}_k - \sigma\mathbf{q}||_2 = \sigma - (\sigma - \mathbf{s}_k) = \mathbf{s}_k$.

Based on the above statement, the pseudo code of the main steps of L_1-L_2 via FBS algorithm is given in Algorithm 1.

Algorithm 1: L_1-L_2 via FBS algorithm

Input: Sensitivity matrix **A**, Regulation parameters λ, Surface photon distribution $\mathbf{\Phi}$,

$t_0 = 1$, $\mathbf{x}_0 = \mathbf{0}$, Maximum iteration numbers $k = 1000$, Minimum residuals $err = 1e - 6$

For $k = 1$ to k do

Step1: Determine the search point by forward splitting: $\mathbf{s}_k = \mathbf{x}_{k-1} - t_{k-1}f'(\mathbf{x}_{k-1})$

Step2: Calculate the approximate solution of Eq. (7) by backward splitting,

the analytical solution as follows:

$\sigma = t_{k-1}\lambda$

if $|\mathbf{s}_k|_\infty>\sigma$

Based on Eq. (13), calculate $\mathbf{z} = soft(\mathbf{s}_k, \sigma)$; $\mathbf{x}_k = \mathbf{z}(||\mathbf{z}||_2 + \sigma)/\,||\mathbf{z}||_2$,

else

$$\mathbf{x}_k = \begin{cases} 0 & if \quad |{\mathbf{s}_k}^i| \leq |\mathbf{s}_k|_\infty \\ |\mathbf{s}_k|_\infty & if \quad |{\mathbf{s}_k}^i| = |\mathbf{s}_k|_\infty, i = \min\left\{i, |{\mathbf{s}_k}^i| = |\mathbf{s}_k|_\infty\right\} \end{cases}$$

if $||\mathbf{x}_k - \mathbf{x}_{k-1}||_2<err$;

break

$t_k = \frac{||\mathbf{x}_k-\mathbf{x}_{k-1}||_2}{2||\nabla f(\mathbf{x}_k)-\nabla f(\mathbf{x}_{k-1})||_2}$

End for

Biomedical Optics EXPRESS

3. Experiments setting

3.1. Numerical simulations

A series of numerical simulations based on the head of the common digital mouse model were conducted to evaluate the performance of L_1-L_2 via FBS algorithm, as shown in Fig. 1(a). The mouse head was segmented into three organs: the muscle, skull, and brain. Their related optical properties list in Table 1, with an excited light wave length is $750nm$ and an emission wavelength is $820nm$ [10]. Figure 1(b) shows the distribution of four excitation source, which were located one transport mean free path beneath the surface on the plane of $z = 18mm$.

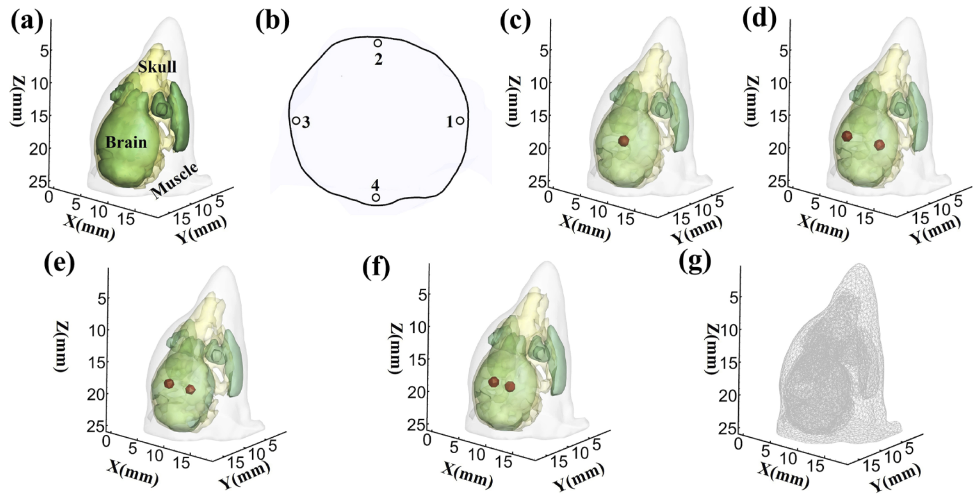

Fig. 1. (a) 3D views the head of a digital mouse. (b) Excitation sources on the plane of $z = 18mm$. The four black circles denote the point excitation sources. (c) The views of simulation models with the single source. (d)-(f) The views of simulation models with the double source, where the edge-to-edge distance between the two source is different. (g) The mesh for inverse reconstruction.

Table 1. Optical parameters in numerical simulation and *in-vivo* experiments

Material	μ_{ax}	μ'_{sx}	μ_{am}	μ'_{sm}
Muscle	0.0474	0.3122	0.0287	0.2427
Skull	0.0326	2.1140	0.0197	1.8541
Brain	0.0183	1.3784	0.0167	1.2156

In order to verify the feasibility of the L_1-L_2 via FBS algorithm, single and double source experiments were designed in feasible experiment. In the single source experiment, one sphere fluorescent source with a $1mm$ radius placed in the brain with center at $(9, 13, 18mm)$, as shown in Fig. 1(c). In double sources experiment, two sphere fluorescent sources with a $1mm$ radius are placed in the center positions placed at $(6, 13, 18mm)$ and $(12, 13, 18mm)$ respectively, shown in Fig. 1(d).

In addition, to verify the robustness of our proposed algorithm, two groups of numerical simulations were conducted by considering the number of excitation sources and the edge-to-edge distance between two sphere fluorescent sources in robustness experiment. Firstly, in the single source experiments, the number of the excitation sources was decrease to two (1 and 3 was used) and one (1 was used), respectively. Secondly, in the double source experiments, two sphere fluorescent sources with a $1mm$ radius were placed at $(6, 13, 18mm)$ and $(11, 13, 18mm)$, the

Biomedical Optics EXPRESS

edge-to-edge distance (EED) was $2mm$, as shown in Fig. 1(e). Furthermore, the center positions of two sphere fluorescent sources were placed at $(7.5, 13, 18mm)$ and $(10.5, 13, 18mm)$ with the edge-to-edge distance was $1mm$, as shown in Fig. 1(f).

In all numerical simulation experiment,the fluorescent yield $\eta\mu_{af}(r)$ of the fluorescent target was set to be 0.05 mm^{-1}.The digital mouse model was discretized into a tetrahedral mesh through Amria 5.2. A uniform tetrahedral mesh which include 10158 nodes and 52696 tetrahedral elements was used in inverse reconstruction. In addition, we used diffusion approximation model based on FEM to simulate the propagation of light through tissues to obtain specific surface energy distributions. The all-experiment codes were written in MATLAB2020 and were performed on a desktop computer with 2.90 GHz Intel Processor I5-9400F and 16G RAM

3.2. FMT imaging system

In order to acquire the CT data and optical image, an FMT imaging system was adopted in our study. Which consist of three parts: (1) Optical acquisition module mainly was composed of an electron multiplying charge coupled device (EMCCD) camera (iXon Ultra DU-897, Andor), a continuous wave optical laser (BS750-6WGA, BoSion Optoelectronic Technology, CHN) and optical filter (FB820-10, THORLABS, USA). (2) Micro-CT system included a X-tray detector (1512N-C90-HRCC, Dexela, USA), and an X-ray generator (L9181-02 MT2195, HAMAMATSUPHOTONICS, CHN); (3) Control module was consist of a 360-degree motorized turntable (RAK100, Zolix, CHN), and a controller (Zolix Instruments Co., Beijing, CHN). As show in Fig. 2, X-Ray Source, Turntable, and X-Ray Detector placed on the same line. In addition, The EMCCD was perpendicular with this line.

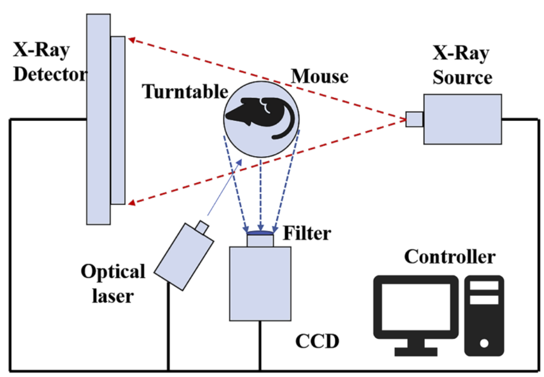

Fig. 2. Our prototype FMT imaging system.

3.3. In-vivo imaging experiment

To further evaluate the performance of L_1-L_2 via FBS algorithm, *in-vivo* glioma mouse experiments were performed. Animal experiments were carried out under isoflurane gas anaesthesia, and every effort was made to relieve the pain of the male mice. Additionally, 5×10^5U-87 MG cells in $6\mu l$ phosphate buffer solution was injected into the brain of the mouse to construct the orthotopic glioma model. After seven days, the tumor-bearing mice were injected with Tf-IRDye800 (excitation spectrum: $750nm$, emission spectrum: $820nm$) via tail vein. Six hours later, fluorescence images and CT data were acquired. And the MRI data obtained subsequently, which was used to determine the location of the tumor.

To provide the excitation illumination, a $750nm$ continuous wave semiconductor laser with the output power of $450mW$ was used was used as the single excited source to reflex excite a fluorescent probe. And an electron multiplying charge coupled device (EMCCD) camera ((iXon

Biomedical Optics EXPRESS

Ultra DU-897, Andor) coupled with 820± 20nm bandpass filter was cooled to −80°C to collect surface fluorescence image with a 120° field of view (FOV). The exposure time (1.6s), high shift speed (12.9us) and high-speed readout rate (10MHz at 16-bit) were set up to restrain the readout noise and the shifting noise. After that, X-ray source was set 70kVp and 39W to obtaining 360° projection data.

Prior to the FMT reconstruction, some essential preprocessing operations were carried out. First, the raw CT data was converted into 3D volume data via the Feldkamp-Davis-Kress (FDK) algorithm for obtaining anatomical structural information. Second, the major organs including muscle, skull and brain were segmented by using Amria 5.2 (Amria, Visage Imaging, Australia). Lastly, the mouse model was discretized into 11504 nodes and 58970 tetrahedral elements for 2D-3D surface energy mapping and FMT reconstruction.

3.4. Algorithm comparison and evaluation index

For comparison, three effective algorithms based on sparse regularization (the L_1-L_2 via DCA, IVTCG, and the ISTA-$L_{1/2}$) were chosen as comparison methods. To promise all algorithms convergent, by experience the maximum iteration numbers and the minimum residuals were set as 1000 and 1e-6, respectively. In addition, to ensure the reliability of the results, the Generalized Cross-Validation method was adopted to determine the regulation parameters λ [39]. The final regularization parameter values for different methods in different experiments have been listed in Table 2.

Table 2. Regularization parameters for different methods in different experiments.

Method	Feasible experiment		Excitation source		EED		*In-vivo* experiment
	Single	Double	two	one	2	1	
FBS	7e0	4e-0	1.05e1	1.05e1	2.5e0	1e0	1e-3
DCA	1e-1	1e-1	0.4e-1	0.8e-1	1e-3	1e-3	5e-0
IVTCG	0.8e0	5e0	1e0	7.5e-3	4e0	1e0	1e1
ISTA-$L_{1/2}$	1e1	5e0	1e1	5.8e0	2e0	3e0	5.8e0

To further quantitative evaluate the accuracy of FBS algorithm in both source location and shape recovery, location error (LE), contrast-to-noise ratio (CNR), means square error RMSE, and Dice index were used as the quantitative indexes. The LE measures the distance variation between the centers of the actual region and the reconstructed region. LE is defined as:

$$LE = ||L_r - L_0||_2 \tag{15}$$

where L_r is the center of the reconstructed area with the highest value in non-zero value of x. L_0 is the barycenter of the real fluorescent area. $||\ .\ ||_2$ is the operator of Euclidean distance. A lower LE index indicates that the reconstruction is better. Dice was introduced to evaluate the similarity of the reconstruction area and the real fluorescent area, which defined as:

$$Dice = \frac{2|s_r \cap s_0|}{|s_r| + |s_0|} \tag{16}$$

where s_r and s_0 represent the reconstruction area and the actual area, respectively. A high dice index indicates that the two regions have better similarities in both location and morphology.More details, the reconstructed fluorescence area was determined by the non-zero tetrahedron region based on x. CNR was performed to demonstrate the contrast of the reconstructed signal and background. Which defined as follows:

$$CNR = \frac{\mu_{ROI} - \mu_{ROB}}{\sqrt{\omega_{ROI}\sigma_{ROI}^2 + \omega_{ROB}\sigma_{ROB}^2}} \tag{17}$$

where ω_{ROI} is the weight coefficient of the region of interest (ROI), and ω_{ROB} is the weight coefficient of the region of back-ground (ROB). μ_{ROI}, σ_{ROI} are the mean values and standard deviations of ROI; μ_{ROI}, σ_{ROB} are the mean values and standard deviations of ROB respectively. A higher CNR value indicates that the source is easier to distinguish from the background. Additionally, RMSE is defined as

$$RMSE = \sqrt{\frac{\sum_N (X_r - X_t)}{N}} \tag{18}$$

where N is the number of nodes, X_r is the reconstructed fluorescence yield, and X_t is the ground truth. A low RMSE means better reconstruction result.

4. Experiment results

4.1. Numerical simulations results

4.1.1. Feasible experiment

Figure 3 showed the reconstruction results of the feasible experiment. Figure 3(a)-(d) and (e)-(h) show the reconstruction results in 3D and transverse view of the single and double source experiment using L_1-L_2 via FBS and three comparing algorithms. In 3D view, the actual and reconstructed fluorescent source were delineated with red meshes and green areas, respectively. Meanwhile, in transverse view the black circles indicated the actual positions of the fluorescent source in the slice of $z = 18mm$. For better evaluated the reconstruction results, reconstructed source center and five quantitative indicators are listed in Table 3.

Table 3. Quantitative results of single and double source reconstruction experiment.

Group	Method	Center (mm)	LE (mm)	Dice	RMSE	CNR	RFY(mm^{-1})
Single	FBS	(9.08, 13.09, 17.82)	0.21	75%	0.00190	34.6	0.050
	DCA	(9.15, 13.20, 17.75)	0.35	60%	0.00202	23.94	0.085
	IVTCG	(9.23, 13.07, 17.76)	0.33	74%	0.00259	12.48	0.090
	ISTA-$L_{1/2}$	(9.34, 13.09, 17.89)	0.37	72%	0.00258	7.47	0.032
Double	FBS	(11.66, 12.79, 18.07)	0.33	69%	0.00237	44.7	0.050
		(6.37, 12.89, 17.82)	0.42				
	DCA	(12.32, 13.28, 18.04)	0.44	36%	0.00253	14.07	0.060
		(6.86, 12.99, 18.12)	0.87				
	IVTCG	(11.68, 12.91, 17.89)	0.34	51%	0.00254	7.03	0.075
		(6.45, 12.85, 17.91)	0.48				
	ISTA-$L_{1/2}$	(11.65, 12.86, 18.09)	0.38	61%	0.00242	19.79	0.065
		(6.43, 12.85, 17.90)	0.46				

From these results, it is obvious that the recovery source by our proposed algorithm is closer the true source compared with other approaches both in single and double source reconstruction. Furthermore, the quantified results in Table 3 also indicate that proposed L_1-L_2 via FBS algorithm achieves the smallest LE and RMSE, and largest Dice similarity and CNR. This indicates that L_1-L_2 via FBS algorithm is feasible and more suited for the application of early tumor detection.

Biomedical Optics EXPRESS

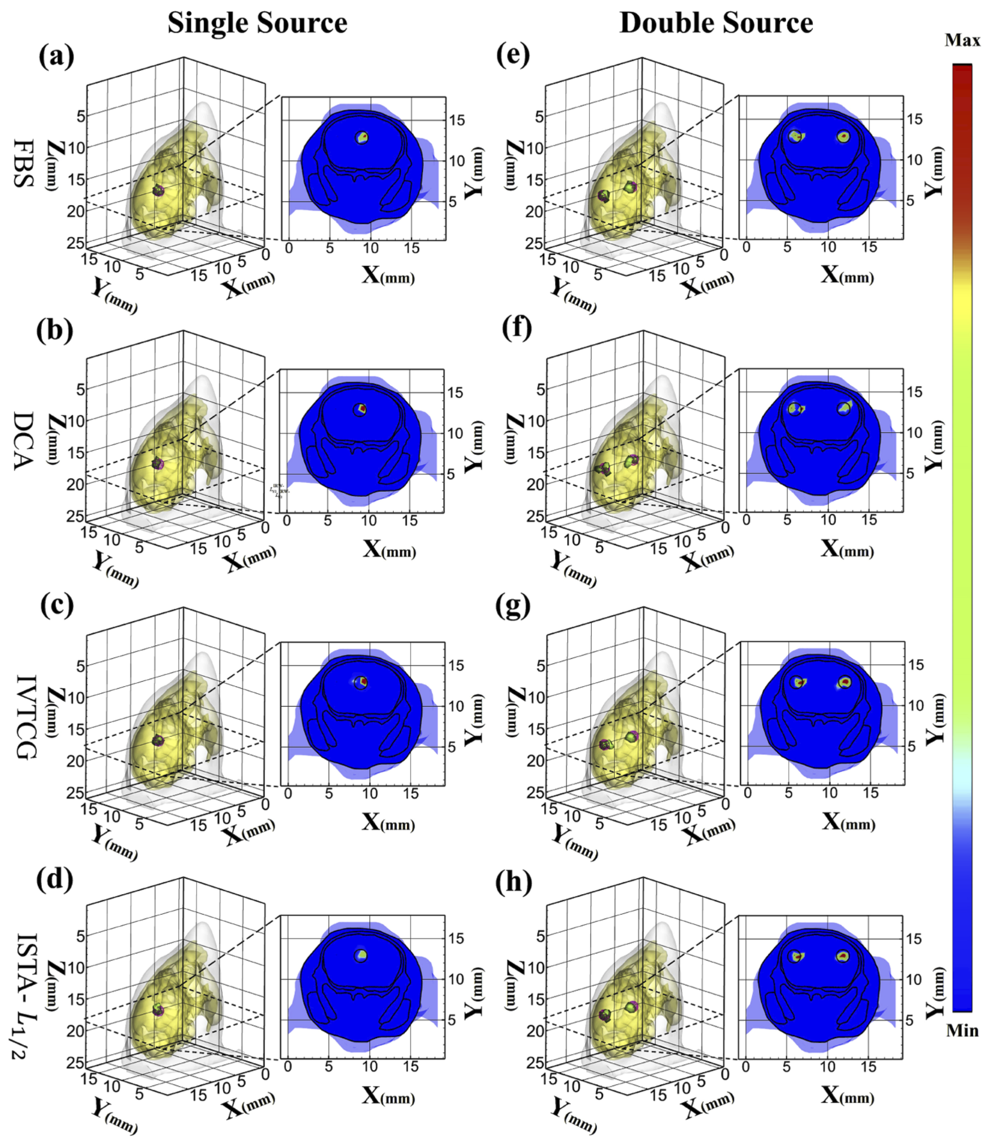

Fig. 3. Result of the feasible experiments (a)-(d) 3D-view and transverse view of the single source reconstructed results (e)-(h) 3D-view and transverse view of the double sources reconstructed results, with the edge-to-edge distance was $4mm$. In 3D view, green areas denote the reconstructed fluorescent sources and red grid represent actual fluorescent source. In transverse view, the black circles represent the actual sources in the slice over the centers of the sources at $z = 18mm$.

However, in slice views, L_1-L_2 via DCA have some location deviation in x-axis as shown in Fig. 3(b) and Fig. 3(f), which resulted in some artifacts and poor shape recovery performance with smallest Dice similarity and largest location errors. In particular, LE obtained by L_1-L_2 via DCA in double source reconstruction is the worst because of the discrete artifacts around the left source. Meanwhile, in double source reconstruction, compare with L_1-L_2 via FBS algorithm, two sources given by IVTCG and ISTA-$L_{1/2}$ algorithm have a little tendency to move towards the center with some location deviation from actual area, as shown in Fig. 3(e) and (h). In addition,

Biomedical Optics EXPRESS

in single source reconstruction, ISTA-$L_{1/2}$ algorithm has some deviation in z-axis from the 3D view in Fig. 3(d), which is consistent with the largest LE of 0.37*mm* in Table 3.

4.1.2. Robustness experiment

Figure 4 and Fig. 5 shows the robustness of the L_1-L_2 via FBS algorithm. In Fig. 4(a)-(d) and (e)-(f) show the reconstructed results in 3D view and transverse view with decreasing the number of excitation source. The corresponding quantitative indicators are presented in Table 4. With the reduction of the number of excitation source, although the reconstruction precision has some different degrees of deterioration, the location error and Dice similarity of all four algorithms can be kept within 0.6*mm* and above 58% in two excitation source case. When one excitation source used, location error and Dice similarity of $L_1 - L_2$ via FBS is still 0.28*mm* and 73% without much deterioration compared with that in 4 excitation source. However, the offset of the green reconstructed area in Fig. 4(f), (g), and (h) are obvious compared with the left corresponding figures. When have one excited source, the location error and Dice similarity of these three contrast algorithm are floating about 0.2*mm* and 6% than that in two excited source. The worst of it is that the Dice similarity of IVTCG is decrease to 35% with a significant shape information losing. In a word, compare with other algorithms, L_1-L_2 via FBS algorithm is more robust in terms of location error and Dice similarity when the number of excited sources is decreased.

Table 4. Quantitative results of different number excitation source experiment.

Method	Exicite source	Center (*mm*)	LE(*mm*)	Dice	RMSE	CNR	RFY(mm^{-1})
FBS	two	(9.07, 12.96, 17.73)	0.21	74%	0.00191	41.19	0.053
	one	(9.11, 13.10, 17.86)	0.28	73%	0.00196	26.27	0.054
DCA	two	(9.19, 12.74, 17.58)	0.52	60%	0.00202	26.32	0.075
	one	(9.13, 13.63, 17.85)	0.70	54%	0.00199	23.67	0.075
IVTCG	two	(9.14, 12.79, 17.69)	0.39	70%	0.00186	26.72	0.050
	one	(8.72, 12.65, 18.39)	0.58	58%	0.00201	11.49	0.036
ISTA-$L_{1/2}$	two	(9.21, 12.80, 17.63)	0.46	58%	0.00199	29.07	0.065
	one	(8.70, 12.63, 18.43)	0.63	53%	0.00197	13.40	0.011

Furthermore, the robustness in double source reconstruction were proved by Fig. 5 and Table 5. Figure 5(a)-(d) and (e)-(h) show the results in 3D view and transverse view of the different edge-to-edge distance experiment.The reconstruction challenges increased with decreasing edge-to-edge distance. And these robustness experiment also reflects the spatial resolving capability. From these results, we can see that L_1-L_2 via FBS algorithm can distinguish two source with edge-to-edge distance of 1*mm* clearly, as shown in Fig. 5(e). Meanwhile, the average location error and Dice of L_1-L_2 via FBS can reach 0.35*mm* and 63% with a good performance in terms of location accuracy, shape recovery capability. In addition, from a series of comparative results, the performance of ISTA-$L_{1/2}$ would be the second-best in terms of LE and Dice. However, the reconstructed image of L_1-L_2 via DCA were blurred with some image artifacts even when edge-to-edge distance was 2*mm*, as shown in Fig. 5(b). Thus, the corresponding Dice, CNR and LE were worst in Table 5. From Fig. 5(f), two sources given by L_1-L_2 via DCA cannot be distinguish because of many existing discrete artifacts. Similarly to Fig. 3(f), the two reconstructed source have a tendency to move towards the center when edge-to-edge distance is 2*mm*. These tendencies are even more pronounced when the edge-to-edge distance is 1*mm* as shown in Fig. 5(g). In conclusion, all these results demonstrated that the L_1-L_2 via FBS algorithm have a best robustness in dual-sources resolution.

Biomedical Optics EXPRESS

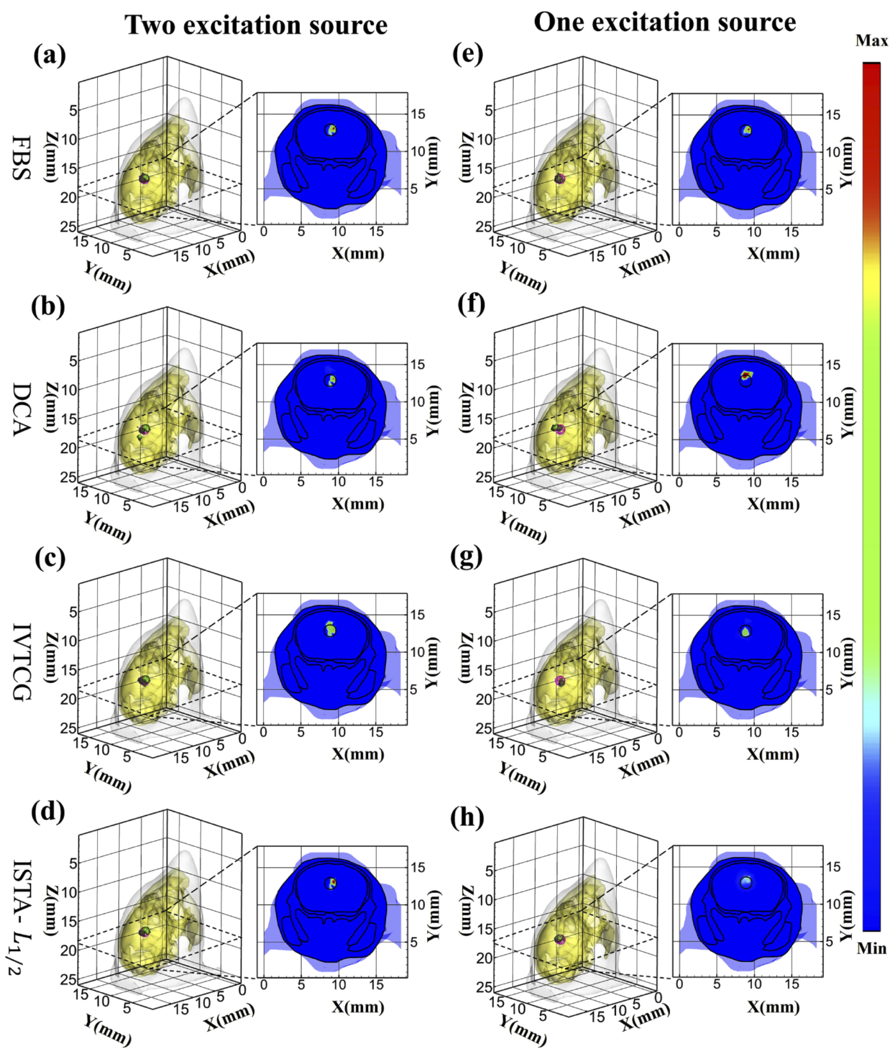

Fig. 4. Result of the different number excite source experiment (a)-(d) 3D-view and transverse view of two excitation source experiment results (e)-(h) 3D-view and transverse view of the one excitation sources experiment results. In 3D view, green areas denote the reconstructed fluorescent sources and red grid represent actual fluorescent source. In transverse view, the black circles represent the actual sources in the slice over the centers of the sources at $z = 18mm$.

4.1.3. In-vivo imaging experiment

In *in-vivo* imaging experiments, to determine the actual source region, MRI image was adopted to draw the outline of the glioma. The reconstructed results of four comparing algorithm in 3D view, transverse view were displayed in Fig. 6(a)-(d), respectively. The reconstructed images in the CT coordinate system were merged with the MRI slice, as shown in Fig. 6(e)-(h). The registration process can divide into three steps: First, by using bwperim and imfill function in MALTAB, we obtained the contour of the CT and MRI images; Second, we used imshowpair and imregconfig function in MALTAB to obtain the optimization metrics and registration parameters; Third, CT and MRI image was put into imregister function and conducted MRI/CT registration based on

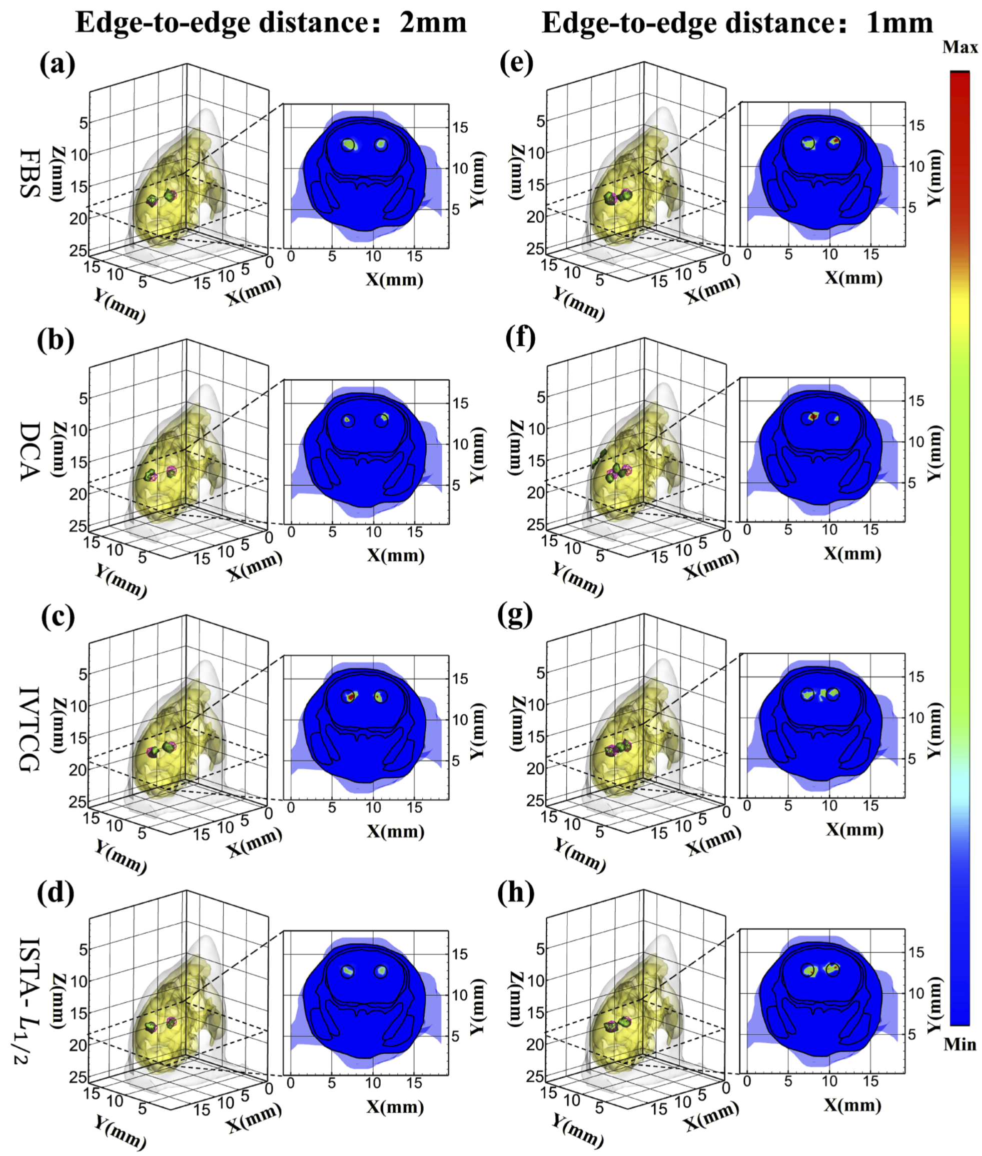

Fig. 5. Result of the different edge-to-edge distance experiment (a)-(d) 3D-view and transverse view of the edge-to-edge distance was $2mm$ experiment results (e)-(h) 3D-view and transverse view of the edge-to-edge distance was $1mm$ experiment results. In 3D view, green areas denote the reconstructed fluorescent sources and red grid represent actual fluorescent source. In transverse view, the black circles represent the actual sources in the slice over the centers of the sources at $z = 18mm$.

the obtained optimization metrics. The white outline is the registration results of the contour of cross-sectional images in the plane $z = 17mm$. And the color area and blue dotted line represent the reconstruction tumor region and the actual tumor margin. Meanwhile, to analyze the results quantitatively, reconstructed source center, LE and Dice were calculated and summarized in Table 6.

According to the *in-vivo* reconstruction results, the tumors were successfully reconstructed using four different approaches. However, for L_1-L_2 via DCA and IVTCG algorithm, the

Biomedical Optics EXPRESS

Table 5. Quantitative results of different edge-to-edge distance experiment

Method	Distance(mm)	Center(mm)	LE(mm)	Dice	RMSE	CNR	RFY(mm^{-1})
FBS	2	(10.03, 13.13, 17.57)	0.44	66%	0.00147	35.27	0.050
		(7.06, 13.02, 18.22)	0.23				
	1	(10.70, 12.82, 18.04)	0.37	63%	0.00251	16.47	0.130
		(7.80, 13.05, 18.44)	0.34				
DCA	2	(10.93, 13.23, 17.39)	0.65	42%	0.00252	5.98	0.070
		(7.06, 13.00,18.41)	0.44				
	1	(11.95, 14.93, 16.16)	3.03	35%	0.00304	5.94	0.040
		(8.7, 13.15, 18.25)	0.82				
IVTCG	2	(10.49, 12.83, 17.83)	0.52	55%	0.00174	15.14	0.070
		(7.45,12.94, 17.83)	0.48				
	1	(10.49, 12.66, 17.65)	0.51	49%	0.00259	13.02	0.120
		(7.37, 12.89, 17.91)	0.40				
ISTA-$L_{1/2}$	2	(10.85, 13.24, 17.68)	0.42	60%	0.00154	41.27	0.055
		(7.08, 13.05, 18.44)	0.45				
	1	(10.75, 13.09, 17.57)	0.49	55%	0.00244	10.92	0.060
		(7.08, 13.05, 18.44)	0.48				

Table 6. Quantitative results of *in-vivo* experiment

Method	Center (mm)	LE (mm)	Dice
FBS	(40.48, 40.13, 16.60)	0.21	84%
DCA	(40.65, 39.29, 16.33)	0.52	40%
IVTCG	(40.65, 39.29, 16.33)	0.39	34%
ISTA-$L_{1/2}$	(40.12, 39.26, 15.99)	0.46	70%

reconstructed tumor were tend to brain interior with large location error and small Dice similarity. Fortunately, the reconstructed area obtained by the L_1-L_2 via FBS and ISTA-$L_{1/2}$ algorithm were consistent with the actual tumor area in MRI image, and their Dice value can reach 84% and 70% respectively. However, as can be from Table 6, the location deviation of the ISTA-$L_{1/2}$ algorithm mainly manifest in z-axial with LE of 1.24mm. In general, L_1-L_2 via FBS algorithm showed the best accuracy with the least LE and largest Dice similarity. These results further revealed the superior performance of L_1-L_2 via FBS in obtaining the morphology and location tracking of the *in-vivo* fluorescence probe distribution in orthotopic glioma mouse models.

Biomedical Optics EXPRESS

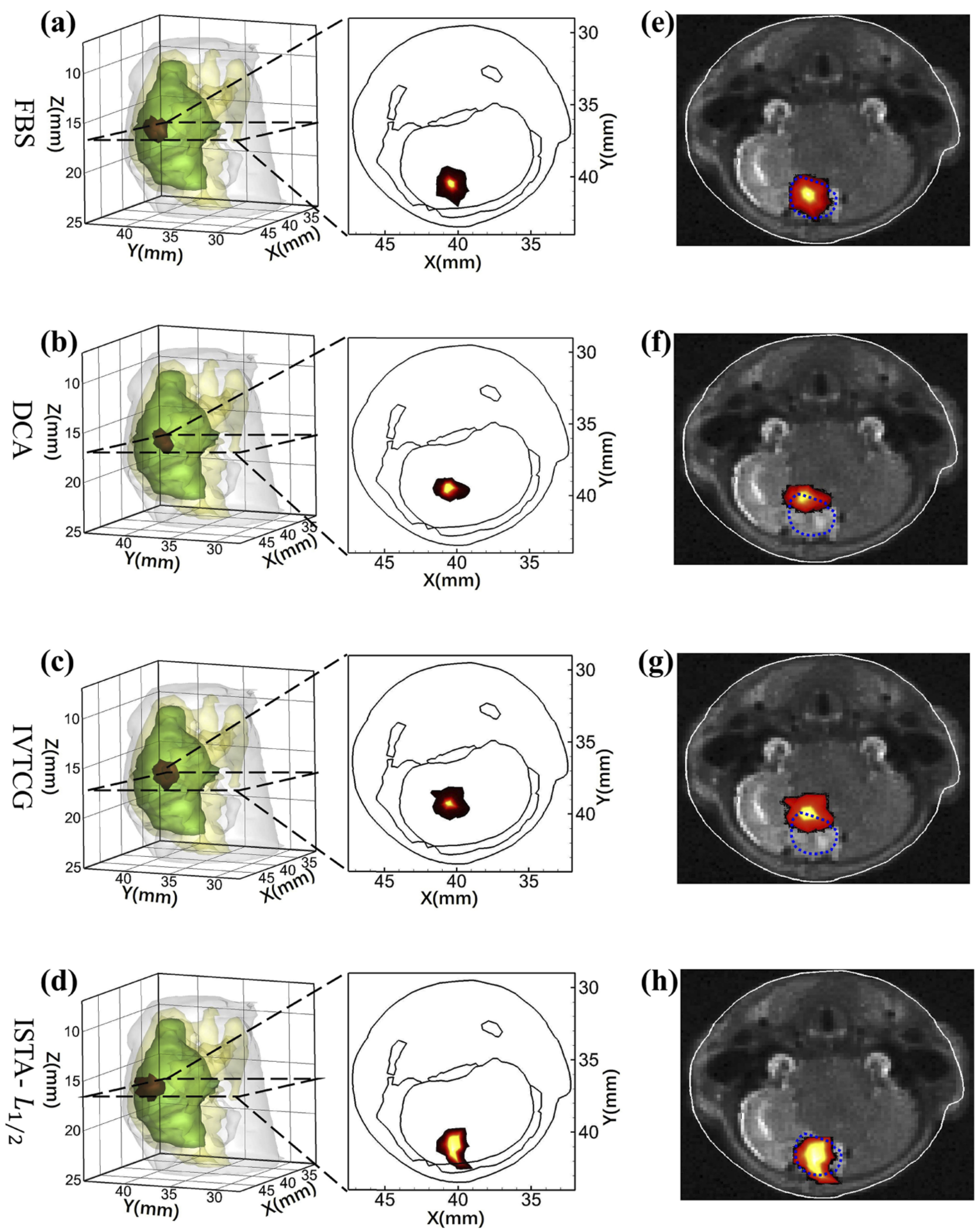

Fig. 6. Reconstruction results of the *in-vivo* experiments. (a)-(d) 3D-view and transverse view of *in-vivo* experiment result. (e)-(h) Images fused by the transverse view and MRI image. In 3D-view the red areas represent reconstruction result. In fused images the white curve is the contour of cross-sectional images, the red area is the reconstruction result, and the blue dotted line outlines the actual location of the tumor.

5. Discussion and conclusion

As a promising preclinical imaging technique, FMT has been paid much attention in imaging theories, acquisition equipment, and biomedical applications. However, because of the severe ill-posedness of inverse reconstruction, the accuracy has limited in many biomedical applications. In this work, a novel L_1-L_2 norm regularization via forward-backward splitting (L_1-L_2 via FBS)

Biomedical Optics EXPRESS

method was proposed for better recovering the 3D distributions of early tumor. Theoretically, L_1-L_2 via FBS algorithm employ proximity operators and gradient descent to obtain the search point and full consider the highly coherent of the system matrix of FMT. Meanwhile, it handles non-differentiable objectives and non-convex constraints caused by L_1-L_2 via FBS norm by splitting the objective to be minimized into simpler functions that are dealt with individually. Thus, L_1-L_2 via FBS method outperforms L_p-norm ($0<p<1$) and L_1-norm in terms of promoting sparsity when sensitivity matrix A is highly coherent. Furthermore, FBS iterations are convergence and not trapped at stationary points, which can guarantee the robust of the solution.

To validate the performance of the proposed L_1-L_2 via FBS algorithm, numerical simulations and *in-vivo* experiments were conducted. L_1-L_2 via DCA, IVTCG and ISTA-$L_{1/2}$ were employed for qualitative and quantitative comparisons. In numerical simulations, feasibility and robustness experiments were conducted. The feasibility experiment results show that L_1-L_2 via FBS algorithm has a best performance in terms of location error and Dice similarity both in single and double source experiment. Which demonstrated the advantage of L_1-L_2 via FBS algorithm in location accuracy, and morphology recovery for early tumor detection. In robustness experiments, with the gradually reducing of the excitation source, the ill-posedness of FMT reconstruction is aggravated. Fortunately, the performance of the L_1-L_2 via FBS algorithm was still satisfactory. Even in the extreme case where only one excited node was used, the proposed algorithm still successfully recovered the source with a deviation of $0.21mm$. Which demonstrates that the accuracy of location and morphology of the proposed algorithm remained steady. And it also indicates the potential of the L_1-L_2 via FBS algorithm in single view FMT reconstruction. By considering the application requirements for multiple tumor detection, with the edge-to-edge distance decreasing, the spatial resolving capability of inverse reconstruction algorithms was verified in another robustness experiments. From these results, we can see that the L_1-L_2 via FBS algorithm can distinguish two sources with an edge-to-edge distance of 1 mm clearly. While, the tumor region reconstructed by the comparison algorithms exhibited problems of inaccuracy, spatial discontinuity and image blur with some image artifacts. Lastly, in *in-vivo* experiment, tumor-bearing mouse model was developed to further evaluate the practicability of L_1-L_2 via FBS algorithm. The *in-vivo* experimental results exhibited that L_1-L_2 via FBS algorithm was great practicality for early tumor detection of living animals. And compared to the other methods, the region reconstructed using L_1-L_2 via FBS algorithm was a better approximation of the actual tumor distribution. It further revealed the superior performance of L_1-L_2 via FBS algorithm in obtaining the morphology and location tracking of the *in-vivo* fluorescence probe distribution. In summary, this result demonstrates the usefulness of the L_1-L_2 via FBS algorithm in resolving multiple sources and improving reconstruction quality and spatial resolution.

It needs to be emphasized that in this work, the absorption and scattering coefficients assigned to each organ were estimated on the basis of a compilation of relevant tissue optical property data reported in the literature [40]. In the pre-clinical practical application, the educated guesses of the optical properties will influence the accuracy of the reconstructed results. In order to solve this problem, some more effective measuring method, like diffusion optical tomography (DOT) [41], or some other near infrared imaging method will be adopted to measure the optical properties of tissue and background. Based on that, in *in-vivo* experiment, the reconstruction accuracy of our proposed algorithm will be further improved. Besides that, due to the lack of absolute calibration technique for photon number and the standard for determining the distribution of tumors in living animals, in *in-vivo* experiment, we did not quantify the CNR and RMSE. In the future, based on the integrating sphere method [42], it is necessary to quantify the reconstruction results precisely by adopting some quantitative analysis method and multimodal imaging technology.

Although L_1-L_2 via FBS algorithm has achieved much better results, the work on this breed of algorithms is far from done, as there are various analysis questions that remain open. Firstly, in our research, L_1-L_2 was limited by the equal penalty for the L_1 and L_2 norms. Considering

Biomedical Optics EXPRESS

the versatility, it can be generalized by considering the L_1-αL_2 metric for $\alpha \geq 0$ in further work. Secondly, an analytical solution for the proximal operator of the L_1-L_2 metric was derived, leading to classical fast L_1 norm solvers such as fast iterative soft-thresholding algorithm and alternating direction method of multipliers (ADMM) that is applicable for L_1-L_2 norm. Therefore, some comparison study will be conducted to confirm the efficient of these optimal algorithms. Lastly, our research mainly focus on the application of FMT in early tumor detection. For some other preclinical application, the types of probe distributions will have a significant difference, which may reduce the performance of our proposed sparse regularization algorithm in some degree. In this case, L_1-L_2 norm should be coupled with some other non-sparse regularization terms to recovery the continuous bigger area probe distributions.

In conclusion, a novel L_1-L_2 norm regularization via forward-backward splitting method was proposed to improve the reconstruction accuracy of FMT in this paper. The L_1-L_2 norm regularization was designed by full considering the highly coherent of the system matrix of FMT and maintaining the simplicity of gradient descent algorithms and the sparsity of results. Compared with several sparse reconstruction algorithms, L_1-L_2 via FBS algorithm performs better in terms of location accuracy, dual-source resolution capability, robustness and in vivo practicability. We believed that this study would promote the preclinical and clinical applications of FMT in early tumor detection.

Funding. National Outstanding Youth Science Fund Project of National Natural Science Foundation of China (11871321, 61901374, 61906154, 61971350); Natural Science Foundation of Shaanxi Province (2019JQ-724); Postdoctoral Innovative Talents Support Program (BX20180254); Scientific and Technological projects of Xi'an (201805060ZD11CG44); Key Research and Development Program of Shaanxi (2020SF-036); Xi'an Science and Technology Project (2019218214GXRC018CG019-GXYD18.3).

Acknowledgment. The authors would like to thank the CAS key Laboratory of Molecular Imaging for *in-vivo* experiment data.

Disclosures. The authors declare no potential conflict of interests.

Data availability. Data underlying the results presented in this paper are not publicly available at this time but may be obtained from the authors upon reasonable request

References

1. V. Ntziachristos, C. Bremer, and R. Weissleder, "Fluorescence imaging with near-infrared light: new technological advances that enable in vivo molecular imaging," European Radiology **13**(1), 195–208 (2003).
2. R. Weissleder, "Scaling down imaging: molecular mapping of cancer in mice," Nat. Rev. Cancer **2**(1), 11–18 (2002).
3. C. Chi, Y. Du, J. Ye, D. Kou, J. Qiu, J. Wang, J. Tian, and X. Chen, "Intraoperative imaging-guided cancer surgery: from current fluorescence molecular imaging methods to future multi-modality imaging technology," Theranostics **4**(11), 1072–1084 (2014).
4. M. Koch, P. Symvoulidis, and V. Ntziachristos, "Tackling standardization in fluorescence molecular imaging," Nat. Photonics **12**(9), 505–515 (2018).
5. V. Ntziachristos, J. Ripoll, L. V. Wang, and R. Weissleder, "Looking and listening to light: the evolution of whole-body photonic imaging," Nat. Biotechnol. **23**(3), 313–320 (2005).
6. L. Kong, Y. An, Q. Liang, L. Yin, Y. Du, and J. Tian, "Reconstruction for fluorescence molecular tomography via adaptive group orthogonal matching pursuit," IEEE Trans. Biomed. Eng. **67**(9), 2518–2529 (2020).
7. J. K. Willmann, N. Van Bruggen, L. M. Dinkelborg, and S. S. Gambhir, "Molecular imaging in drug development," Nat. Rev. Drug Discovery **7**(7), 591–607 (2008).
8. A. Ale, V. Ermolayev, E. Herzog, C. Cohrs, M. H. De Angelis, and V. Ntziachristos, "Fmt-xct: in vivo animal studies with hybrid fluorescence molecular tomography–x-ray computed tomography," Nat. Methods **9**(6), 615–620 (2012).
9. X. He, H. Meng, X. He, K. Wang, X. Song, and J. Tian, "Nonconvex laplacian manifold joint method for morphological reconstruction of fluorescence molecular tomography," Mol Imaging Biol **23**(3), 394–406 (2021).
10. H. Meng, K. Wang, Y. Gao, Y. Jin, X. Ma, and J. Tian, "Adaptive gaussian weighted laplace prior regularization enables accurate morphological reconstruction in fluorescence molecular tomography," IEEE Trans. Med. Imaging **38**(12), 2726–2734 (2019).
11. A. Jin, B. Yazici, A. Ale, and V. Ntziachristos, "Preconditioning of the fluorescence diffuse optical tomography sensing matrix based on compressive sensing," Opt. Lett. **37**(20), 4326–4328 (2012).
12. H. Meng, Y. Gao, X. Yang, K. Wang, and J. Tian, "K-nearest neighbor based locally connected network for fast morphological reconstruction in fluorescence molecular tomography," IEEE Trans. Med. Imaging **39**(10), 3019–3028 (2020).

Biomedical Optics EXPRESS

13. X. He, X. Wang, H. Yi, Y. Chen, X. Zhang, J. Yu, and X. He, "Laplacian manifold regularization method for fluorescence molecular tomography," J. Biomed. Opt. **22**(4), 045009 (2017).
14. H. Wang, C. Bian, L. Kong, Y. An, Y. Du, and J. Tian, "A novel adaptive parameter search elastic net method for fluorescent molecular tomography," IEEE Trans. Med. Imaging **40**(5), 1484–1498 (2021).
15. S. Zhang, X. Ma, Y. Wang, M. Wu, H. Meng, W. Chai, X. Wang, S. Wei, and J. Tian, "Robust reconstruction of fluorescence molecular tomography based on sparsity adaptive correntropy matching pursuit method for stem cell distribution," IEEE Trans. Med. Imaging **37**(10), 2176–2184 (2018).
16. H. Guo, X. He, M. Liu, Z. Zhang, Z. Hu, and J. Tian, "Weight multispectral reconstruction strategy for enhanced reconstruction accuracy and stability with cerenkov luminescence tomography," IEEE Trans. Med. Imaging **36**(6), 1337–1346 (2017).
17. H. Guo, J. Yu, Z. Hu, H. Yi, Y. Hou, and X. He, "A hybrid clustering algorithm for multiple-source resolving in bioluminescence tomography," J. Biophotonics **11**(4), e201700056 (2018).
18. Y. Zhou, M. Chen, H. Su, and J. Luo, "Self-prior strategy for organ reconstruction in fluorescence molecular tomography," Biomed. Opt. Express **8**(10), 4671–4686 (2017).
19. N. Cao, A. Nehorai, and M. Jacob, "Image reconstruction for diffuse optical tomography using sparsity regularization and expectation-maximization algorithm," Opt. Express **15**(21), 13695–13708 (2007).
20. S. Jiang, J. Liu, G. Zhang, Y. An, H. Meng, Y. Gao, K. Wang, and J. Tian, "Reconstruction of fluorescence molecular tomography via a fused lasso method based on group sparsity prior," IEEE Trans. Biomed. Eng. **66**(5), 1361–1371 (2019).
21. Y. Lu, X. Zhang, A. Douraghy, D. Stout, J. Tian, T. F. Chan, and A. F. Chatziioannou, "Source reconstruction for spectrally-resolved bioluminescence tomography with sparse a priori information," Opt. Express **17**(10), 8062–8080 (2009).
22. D. Han, J. Tian, S. Zhu, J. Feng, C. Qin, B. Zhang, and X. Yang, "A fast reconstruction algorithm for fluorescence molecular tomography with sparsity regularization," Opt. Express **18**(8), 8630–8646 (2010).
23. A. Beck and M. Teboulle, "A fast iterative shrinkage-thresholding algorithm for linear inverse problems," SIAM J. Imaging Sci. **2**(1), 183–202 (2009).
24. Y. Liu, J. Yu, X. Qin, and J. Guo, "The split bregman iteration algorithm for bioluminescence tomography," Sci. Sin.-Inf. **44**(2), 284–294 (2014).
25. C. Leng, D. Yu, S. Zhang, Y. An, and Y. Hu, "Reconstruction method for optical tomography based on the linearized bregman iteration with sparse regularization," Computational and mathematical methods in medicine **2015**, 1–8 (2015).
26. X. He, J. Yu, X. Wang, H. Yi, Y. Chen, X. Song, and X. He, "Half thresholding pursuit algorithm for fluorescence molecular tomography," IEEE Trans. Biomed. Eng. **66**(5), 1468–1476 (2019).
27. H. Guo, Z. Hu, X. He, X. Zhang, M. Liu, Z. Zhang, X. Shi, S. Zheng, and J. Tian, "Non-convex sparse regularization approach framework for high multiple-source resolution in cerenkov luminescence tomography," Opt. Express **25**(23), 28068–28085 (2017).
28. Y. Lou, P. Yin, Q. He, and J. Xin, "Computing sparse representation in a highly coherent dictionary based on difference of l_1 and l_2," J Sci Comput **64**(1), 178–196 (2015).
29. H. Zhang, G. Geng, X. Wang, X. Qu, Y. Hou, and X. He, "Fast and robust reconstruction for fluorescence molecular tomography via regularization," BioMed Res. Int. **2016**, 1–9 (2016).
30. Y. Lou and M. Yan, "Fast l1–l2 minimization via a proximal operator," J Sci Comput **74**(2), 767–785 (2018).
31. X. Zhang, W. Zhou, X. Zhang, and H. Gao, "Forward–backward splitting method for quantitative photoacoustic tomography," Inverse problems **30**(12), 125012 (2014).
32. Q. Ding, G. Chen, X. Zhang, Q. Huang, H. Ji, and H. Gao, "Low-dose ct with deep learning regularization via proximal forward–backward splitting," Phys. Med. Biol. **65**(12), 125009 (2020).
33. X. He, J. Liang, X. Wang, J. Yu, X. Qu, X. Wang, Y. Hou, D. Chen, F. Liu, and J. Tian, "Sparse reconstruction for quantitative bioluminescence tomography based on the incomplete variables truncated conjugate gradient method," Opt. Express **18**(24), 24825–24841 (2010).
34. A. X. Cong and G. Wang, "A finite-element-based reconstruction method for 3d fluorescence tomography," Opt. Express **13**(24), 9847–9857 (2005).
35. M. Schweiger, S. Arridge, M. Hiraoka, and D. Delpy, "The finite element method for the propagation of light in scattering media: boundary and source conditions," Med. Phys. **22**(11), 1779–1792 (1995).
36. D. Wang, X. Liu, Y. Chen, and J. Bai, "A novel finite-element-based algorithm for fluorescence molecular tomography of heterogeneous media," IEEE Trans. Inform. Technol. Biomed. **13**(5), 766–773 (2009).
37. Y. Lv, J. Tian, W. Cong, G. Wang, J. Luo, W. Yang, and H. Li, "A multilevel adaptive finite element algorithm for bioluminescence tomography," Opt. Express **14**(18), 8211–8223 (2006).
38. T. K. Pong, P. Tseng, S. Ji, and J. Ye, "Trace norm regularization: reformulations, algorithms, and multi-task learning," SIAM J. Optim. **20**(6), 3465–3489 (2010).
39. H. Liao and M. K. Ng, "Blind deconvolution using generalized cross-validation approach to regularization parameter estimation," IEEE Trans. on Image Process. **20**(3), 670–680 (2011).
40. G. Alexandrakis, F. R. Rannou, and A. F. Chatziioannou, "Tomographic bioluminescence imaging by use of a combined optical-pet (OPET) system: a computer simulation feasibility study," Phys. Med. Biol. **50**(17), 4225–4241 (2005).

Biomedical Optics EXPRESS

41. W. Lu, J. Duan, D. Orive-Miguel, L. Herve, and I. B. Styles, "Graph-and finite element-based total variation models for the inverse problem in diffuse optical tomography," Biomed. Opt. Express **10**(6), 2684–2707 (2019).
42. O. A. Savchuk, J. Carvajal, J. Massons, M. Aguiló, and F. Díaz, "Determination of photothermal conversion efficiency of graphene and graphene oxide through an integrating sphere method," Carbon **103**, 134–141 (2016).